







Trapping and escape of viscous fingers in a soft Hele-Shaw cell

Gunnar G. Peng ^{1,2} Callum Cuttle ³ Finn Box ² Jian Hui Guan,^{3,4} Anne Juel ²
Christopher W. MacMinn ³ and Draga Pihler-Puzović ²

¹*Department of Mathematics, Imperial College London, Exhibition Road,
London SW7 2BX, England, United Kingdom*

²*Department of Physics and Astronomy and Manchester Centre for Nonlinear Dynamics,
University of Manchester, Oxford Road, Manchester M13 9PL, England, United Kingdom*

³*Department of Engineering Science, University of Oxford, Parks Road,
Oxford OX1 3PJ, England, United Kingdom*

⁴*Department of Mathematics, The University of North Carolina at Chapel Hill, Chapel Hill,
North Carolina 27599, USA*



(Received 7 March 2022; accepted 12 May 2022; published 8 June 2022)

Viscous flow in the narrow gap between a rigid plate and a confined elastic solid has been observed to “choke” at high flow rates, due to the deforming solid making contact with the plate and sealing the gap. When the viscous flow is driven by injection of a gas bubble, the advancing meniscus is susceptible to the viscous-fingering instability. By comparing fingering experiments with axisymmetric numerical simulations, we demonstrate that, depending on the width of the fingers, the fingering instability can either promote or suppress choking, i.e., cause the system to choke when an axisymmetric system would not, or vice versa.

DOI: [10.1103/PhysRevFluids.7.L062001](https://doi.org/10.1103/PhysRevFluids.7.L062001)

Interactions between interfacial flows and deformable components are encountered frequently in industry and technology. Traditionally, soft components are introduced to systems as a secondary means of modifying interfacial instabilities to our advantage. For example, the Rayleigh-Taylor instability is amplified in solidifying melts to produce soft solids with complex surface geometry [1], while the onset of the ribbing instability during roll coating is suppressed towards larger roll speeds if the rolls are covered by a compliant material [2,3]. More recently, soft components have also become primary in the design of advanced technologies, including nanoscale assembly [4], wearable sensing devices [5,6], and soft robotics [7], where two-phase flows are exploited for fabrication and actuation. A fundamental understanding of the potential interactions between multiphase flows and deformable components is therefore essential, and yet only a handful of model systems have so far been examined.

One such model system with relevance to both soft technological components and interfacial instabilities is a deformable Hele-Shaw cell. A rigid Hele-Shaw cell comprises a narrow gap between two parallel plates. The viscous-fingering instability, which occurs when a gas displaces a viscous liquid between the plates, has been studied extensively as a canonical interfacial instability with relevance to enhanced oil recovery [8] and carbon sequestration [9]. This instability was previously coupled to deformable components by replacing one of the rigid plates with an elastic membrane, creating an *unconfined* soft Hele-Shaw cell, which delayed the onset of the instability [10]. Here, we study a *confined* soft Hele-Shaw cell in which the deformable wall is a volumetrically confined slab of elastomer [see Fig. 1(a)]. A recent study showed that, for steady single-phase injection, a confined soft flow cell behaves as a liquid fuse with possible applications to microfluidics and soft

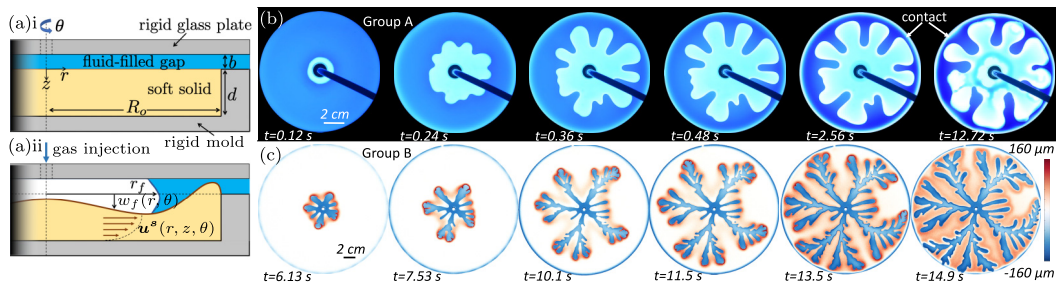


FIG. 1. (a) Schematic of the setup (a)i before and (a)ii after the start of gas injection. Here, $r_f(\theta)$ is the radial extent of the interface, $\mathbf{u}^s(r, \theta, z)$ is the solid displacement vector, and $w_f(r, \theta) = u_z^s(r, \theta, 0)$. (b), (c) Top view of an injected gas bubble displacing viscous liquid in the narrow gap between a glass plate and a confined slab of elastomer. Images taken at different times t after gas injection started. (b) Group A: The liquid is dyed blue, so darker color indicates a thicker layer of liquid. Flow-induced deformation of the elastomer eventually leads to contact between the soft slab and the glass plate in the vicinity of the cell rim (visible as a white band encircling the cell), trapping the viscous fingers within the cell. ($R_o = 60$ mm, $d = 7$ mm, $b = 1.5$ mm, $G = 1.15$ kPa, $\mu = 0.8$ Pa s, $\gamma = 63$ mN/m, $Q_0 = 500$ ml/min.) (The slow dewetting of the film in the bubble region visible in the last panel did not affect the growth of the fingering instability.) (c) Group B: The coloring shows change in liquid-layer thickness relative to the thickness of the initial gap b , with red and blue shades outside the bubble region corresponding to expansion and contraction of the gap, respectively (see color bar). The fingers escape the cell despite constriction near the rim. ($R_o = 95$ mm, $d = 4$ mm, $b = 0.16$ mm, $G = 4.2$ kPa, $\mu = 1.02$ Pa s, $\gamma = 63$ mN/m, $Q_0 = 49.4$ ml/min.)

robotics [11]; mechanically, the elastomer is sheared outwards with the flow and accumulates in a boundary layer near the outlet, which constricts the flow and, above a critical flow rate, “chokes” the flow entirely. We now extend these previous studies by considering two-phase flow in a confined soft flow cell and investigate whether the cell still chokes at a critical flux, and the role of viscous fingering in this process.

Figures 1(b) and 1(c) show two experiments where an injected bubble develops fingers that either become trapped in the choked cell [Fig. 1(b)] or escape the cell, which in turn fails to choke [Fig. 1(c)]. Surprisingly, numerical simulations of axisymmetric bubble expansion in a confined soft flow cell for the same flow rates show the opposite behavior, choking for the parameters of Fig. 1(c), but not those of Fig. 1(b). This difference in choking behavior must be due to the viscous fingering, as the simulations are in quantitative agreement with experiments in cases when fingering is negligible and the interface is nearly circular. Using this comparison between experiments and axisymmetric mathematical modeling, we elucidate the fluid-structure interactions that enable both the trapping and escape of viscous fingers and thus demonstrate a systematic relationship between the outcome and interface morphology.

Two groups of experiments, labeled group A and group B, were performed by the Manchester and Oxford groups, respectively, using radially outward injection into confined soft Hele-Shaw cells [Fig. 1(a)]. Silicone-based elastomer was cured in cylindrical molds of radius R_o and depth d to create nearly incompressible soft slabs with aspect ratio $\mathcal{A}_s = R_o/d$, which remained adhered to, and confined by, the mold. The initial separation distance b between the soft substrate and the overlying glass plate (and the corresponding gap aspect ratio $\mathcal{A}_f = R_o/b$) was set by spacers. The flow cell was prefilled with glycerol, and gas was injected into the prefilled cell through a port in the center of the glass plate at nominal volumetric flow rate Q_0 . The properties of the elastomer (shear modulus G and Poisson’s ratio ν) and glycerol (viscosity μ and surface tension γ) were either measured prior to each experiment or inferred from published data. The evolution of the interface was captured by a camera from above. For group B, the deflection of the whole substrate ahead of the interface was quantified using a custom-built light-attenuation technique (see Supplemental Material [12]).

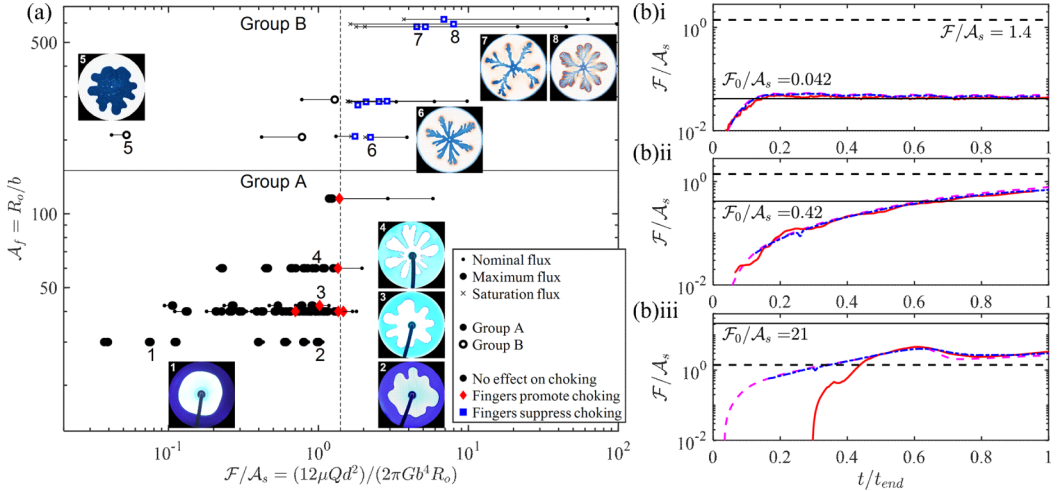


FIG. 2. (a) Phase diagram of experimental results in different soft Hele-Shaw cells in terms of gap aspect ratio $\mathcal{A}_f = R_o/b$ vs nondimensional flow rate $\mathcal{F}/\mathcal{A}_s$ [12]. The quantity $\mathcal{F}/\mathcal{A}_s$ is calculated using both the maximal value of the flow rate $Q(t)$ observed experimentally for $r_f < R_o - d$ (large markers) and the nominal imposed injection flow rate Q_0 (small dots), connected by a horizontal line. The critical value of $\mathcal{F}/\mathcal{A}_s \approx 1.4$, above which the cells would choke for single-phase flow [11], is shown with the vertical dashed line. Marker shapes and colors indicate whether choking occurred in the experiments or in analogous axisymmetric simulations following the experimentally measured $Q(t)$. (In no case did choking occur in both.) A representative selection of instantaneous interface shapes and the corresponding points in the phase diagram are marked with numbers 1 to 8. (b) Typical evolution of the nondimensional flow rate $\mathcal{F}/\mathcal{A}_s$, with time t , normalized by the duration of the experiment t_{end} , for when (i) $\mathcal{F}/\mathcal{A}_s$ settles to the nominal (imposed) value $\mathcal{F}_0/\mathcal{A}_s$ (solid horizontal lines), (ii) $\mathcal{F}/\mathcal{A}_s$ continues growing throughout the experiment, and (iii) $\mathcal{F}/\mathcal{A}_s$ grows before saturating at a value close to the single-phase choking threshold $\mathcal{F}/\mathcal{A}_s \approx 1.4$ (dashed horizontal lines). The saturation flow rate (i.e., the minimum obtained after the peak) is plotted in panel (a) as crosses connected by horizontal lines for the relevant experiments in group B. The data correspond to the experiments done with $R_o = 95$ mm, $d = 4$ mm, $\gamma = 63$ mN/m: (i) $G = 2.9$ kPa, $Q_0 = 1$ ml/min, $b = 0.45$ mm, $\mu = 0.95$ Pa s; (ii) $G = 2.9$ kPa, $Q_0 = 10$ ml/min, $b = 0.46$ mm, $\mu = 1.03$ Pa s; and (iii) $G = 3.9$ kPa, $Q_0 = 11.1$ ml/min, $b = 0.16$ mm, $\mu = 1.01$ Pa s. The time evolution was obtained by time differentiating the volume of fluid in the cell as measured by light attenuation (blue dash-dotted line, group B only), measuring the gas pressure to infer the gas volume (red solid line, various experiments), and inferring the volume of liquid displaced by the advancing meniscus using a traveling-wave model (magenta dashed line, all experiments). The three methods agree, and we therefore choose to report traveling-wave-based measurements in panel (a) [12].

Figure 2(a) summarizes results from more than 150 experiments. The vertical axis is the gap aspect ratio $\mathcal{A}_f = R_o/b$, while the horizontal axis is the nondimensional quantity $\mathcal{F}/\mathcal{A}_s = 12\mu Qd^2/(2\pi Gb^4R_o)$, which can be interpreted as a nondimensional flow rate. Insets of Fig. 2(a) illustrate the range of interface morphologies observed due to viscous fingering. In a rigid cell, fingering would be controlled by two nondimensional parameters: \mathcal{A}_f and the capillary number $\text{Ca} = \mu Q/(2\pi R_o b \gamma)$ (note that Ca is proportional to $\mathcal{F}/\mathcal{A}_s$ by a constant factor $12d^2\gamma/(Gb^3)$ for any given experiment). References [13–15] predict larger growth rates and wave numbers when \mathcal{A}_f and/or Ca increase. Consistent with these expectations, we see more branching and narrower fingers as \mathcal{A}_f and/or $\mathcal{F}/\mathcal{A}_s$ increase [i.e., moving upward and/or to the right in Fig. 2(a)]. For example, compare experiments in the lower left (e.g., inset 1) where the interface remains almost circular to those in the upper right (insets 6–8) where the interface develops long and narrow or highly branched and fractal fingers. Morphologies intermediate to these extremes are shown by insets 2, 3, and 4, obtained at approximately the same $\mathcal{F}/\mathcal{A}_s$ and Ca but increasing \mathcal{A}_f . Hence, traditional rigid-cell

control parameters appear to qualitatively describe the fingering pattern. Notably absent from these results is any evidence that deformation significantly suppresses the instability, as it has been shown to do in unconfined soft flow cells (see Ref. [10]). A prominent feature of our results, absent from both rigid and unconfined soft flow cells, is that the fingers can become trapped by choking around the rim. As discussed above, choking is a key feature of single-phase flow in confined soft flow cells. We next assess the extent to which fingering can promote or suppress this choking phenomenon.

For steady single-phase injection, our cells would choke for flow rates above the critical value

$$\mathcal{F}/\mathcal{A}_s \approx 1.4, \quad (1)$$

marked with a vertical dashed line in Fig. 2(a) [11]. This simple picture is not borne out in our system, where in several experiments the flow rate greatly exceeded the threshold without choking [blue squares in Fig. 2(a)], while in experiments that did choke (red diamonds) choking often occurred below the threshold. There are three key differences between our experiments and steady single-phase injection.

(i) The actual injection rate, i.e., the rate of change of gas volume in the cell, varies in time due to the effects of gas compression.

(ii) The pressure drop required to drive the flow decreases with time as gas displaces liquid.

(iii) Viscous fingering generates a nonaxisymmetric interface and flow field.

Before we can assess the impact of fingering [point (iii)], we must understand the effects of points (i) and (ii).

Each experiment is plotted as a small dot in Fig. 2(a), indicating its nominal nondimensional flow rate $\mathcal{F}_0/\mathcal{A}_s = 12\mu Q_0 d^2 / (2\pi G b^4 R_o)$, connected by a horizontal line to a large marker, indicating the maximal flow rate $Q(t)$ observed in the experiment. We measured $Q(t)$ in the experiments using three different methods, all of which agreed [see Fig. 2(b) and Supplemental Material [12]]. The time evolution of $Q(t)$ is caused by gas compression, and is significant for small gap b or large nominal flow rate Q_0 . Specifically, $Q(t)$ is delayed in reaching Q_0 while gas in the bubble is compressed, which pressurizes the bubble and drives flow [see Fig. 2(b)]. The gas eventually depressurizes as the interface advances and the viscous resistance decreases, leading to an overshoot of the flow rate followed by slow decay towards Q_0 [Fig. 2(b)i], although the experiment may end while still in the pressurization phase due to a finger escaping [Fig. 2(b)ii]. For large Q_0 (i.e., $\mathcal{F}_0/\mathcal{A}_s \gg 1.4$), a near-choking state can be obtained, in which a balance between gas compression and constriction near the rim prevents Q from rising above the critical value for single-phase choking given by Eq. (1), although the choking threshold may be transiently exceeded before the constriction is established [Fig. 2(b)iii]. The near-choking state explains the blue points in Fig. 2(a) with maximal $Q(t)$ above the choking threshold. In this regime only, we also use a third marker in Fig. 2(a) (crosses) to show near-choking flow rates [i.e., the minimal measurement after the peak in $Q(t)$], which lie close to the threshold and are well below the nominal flow rate.

To assess the effects of two-phase flow and air compression in the absence of fingering, we use numerical simulations of axisymmetric two-phase displacement in a soft Hele-Shaw cell. The equations of linear elasticity for the elastomer in the domain $0 < r < R_o$, $0 < z < d$,

$$\nabla \cdot \mathbf{u}^s + \frac{3(1-2\nu)}{2(1+\nu)} \frac{p^s}{G} = 0, \quad (2a)$$

$$\nabla \cdot \boldsymbol{\sigma}^s = -\frac{3}{2(1+\nu)} \nabla p^s + G \nabla^2 \mathbf{u}^s = \mathbf{0}, \quad (2b)$$

where \mathbf{u}^s is the displacement vector, $\boldsymbol{\sigma}^s$ is the stress tensor, and $p^s = -\text{Tr}(\boldsymbol{\sigma}^s)/3$ is the solid pressure, were coupled to the depth-averaged lubrication equations for viscous incompressible flow of liquid ($\mathcal{A}_f = R_o/b \gg 1$) in the region $r_f < r < R_o$,

$$\frac{\partial w_f}{\partial t} = \frac{1}{r} \frac{\partial}{\partial r} \left(r \frac{(b+w_f)^3}{12\mu} \frac{\partial p}{\partial r} \right), \quad (3)$$

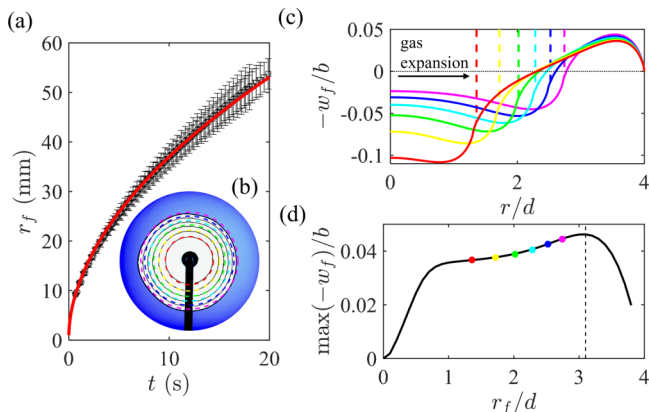


FIG. 3. Direct comparison between experiments and numerics for $R_o = 60$ mm, $d = 15$ mm, $b = 2$ mm, $G = 1.36$ kPa, $\mu = 0.72$ Pa s, $\gamma = 63$ mN/m, and $Q_0 = 50$ ml/min, when the interface remains circular. (a) Time evolution of the interface radius r_f obtained numerically (solid line) and in three separate experimental runs (markers showing average with error bars showing standard deviation). (b) A superposition of instantaneous interfacial shapes obtained experimentally (solid lines) and numerically (dashed lines), with spacing $\Delta t = 1.82$ s starting from $t = 3.26$ s after the start of the injection. (c) Numerically obtained radial profiles of the deflection of the solid free surface scaled by the initial gap thickness, $-w_f/b$, as a function of radial position normalized by the solid thickness, r/d , and the corresponding instantaneous positions of the interface (vertical dashed lines, see also dots in (d)), at the same times as in panel (b). (d) The evolution of the height of the bulge scaled by the initial gap thickness, $\max(-w_f)/b$, as a function of the interface position normalized by the solid thickness, r_f/d . The dashed line indicates the interface position, for which the bulge height starts decreasing. Note that in panels (c) and (d) the rim is at $r/d = r_f/d = 4$.

where $w_f(r, t)$ is the vertical deformation of the cell and $p(r, t)$ is the fluid pressure, while assuming a spatially uniform pressure inside the expanding circular gas bubble with the interface at $r = r_f$. The coupling between the fluid and the elastic substrate was imposed at $z = 0$, by matching w_f and p from the lubrication problem with the z components of \mathbf{u}^s and σ^s from the solid problem, while the shear stress from the fluid onto the solid was neglected. The elasticity equations were subjected to the no-slip boundary conditions on the mold and symmetry conditions at the cell center. At the displacement front $r = r_f(t)$, the kinematic and dynamic boundary conditions were modified to account for residual liquid films [16], and the volumetric flow rate and pressure were imposed at the cell rim [12].

The evolution of the gap constriction at the rim depends on the time evolution of the flow rate $Q(t)$. Even in an axisymmetric system, the flow rate would deviate from its nominal value of Q_0 due to compressibility; fingering contributes to this deviation by modifying the effective viscous resistance. To directly compare a fingering flow with an axisymmetric flow in terms of the resulting impact on choking, we therefore impose the experimentally measured $Q(t)$ in the numerics.

The effects of axisymmetric two-phase flow on the elastomer deformation are illustrated by comparing numerical simulations with an experiment in which the interface remained nearly circular. In this regime, we observe strong quantitative agreement for the time-evolving radius and shape of the interface [Figs. 3(a) and 3(b)]. Numerically, we find that the gradient in pressure that drives the liquid outward also shears the soft slab toward the confining rim [Fig. 3(c)]. This generates the constriction (i.e., the minimum gap) close to the cell rim where sheared material accumulates in a boundary layer [11]. Inside the bubble, the spatially uniform pressure has no shearing effect on the incompressible solid, which consequently relaxes back toward its undeformed state. Near the interface, the cell gap attains its maximum, due to the solid being sheared away from it on the liquid side only. Since the soft solid is adhered to the plate mold, stresses applied to the solid surface only

affect an $O(d)$ region around the point of application, and so the effects of the interface only reach an $O(d)$ length into the liquid region. As the interface approaches within $O(d)$ of the rim, the volume of material sheared toward the rim diminishes and the constriction reduces in size [Fig. 3(d)]. Hence, two-phase flow without fingering acts to suppress choking due to the interaction between the interface and the rim at a distance $O(d)$, which we refer to as the “proximity mechanism.” Viscous fingering should enhance this effect because the complex interface extends closer to the rim than a circular bubble growing at the same rate (see Fig. S1 in Supplemental Material [12]). Indeed, comparing analogous simulations with the high-flow rate experiments in group B [blue squares in Fig. 2(a)], we find that choking is predicted in axisymmetric simulations, yet it is absent in the experiments.

Conversely, we also find evidence that fingering can promote choking, compared with axisymmetric two-phase displacement. Specifically, for the experiments in group A in which choking was observed [red diamonds in Fig. 2(a)], simulations did not choke for the same flow rate $Q(t)$. In the experiments, the nonaxisymmetric flow field generated by the instability increases the local flow ahead of the advancing fingers [relative to the uniformly distributed flow rate $Q/(2\pi R_o)$ in the case of an axisymmetric interface], which can promote localized choking near the rim ahead of the fingers even when the azimuthally averaged flux is below the choking threshold. Once choking occurs locally, the flux increases in all nonchoked regions and the obstruction rapidly spreads around the entire flow cell. The nonaxisymmetry in the flow field decays ahead of the fingers on a length scale comparable to the finger width, so this “focusing mechanism” allows wider fingers to promote choking from a further distance.

Whether fingering promotes or suppresses choking depends on which mechanism is dominant, which itself depends on finger morphology. When the interface is far away from the rim, neither mechanism has an effect. As the interface comes closer, for wider fingers the focusing mechanism has a further reach, so it becomes dominant first and may trigger choking before the bulge is affected enough by the proximity mechanism; for narrower fingers, the reverse is true. At large \mathcal{A}_f , associated with branched and narrow fingers [blue squares in Fig. 2(a)], choking is therefore heavily suppressed even for flow rates beyond the axisymmetric choking threshold. (Additionally, for high flow rates and narrow gaps, the small compressibility of the solid may start to play a role and would also reduce bulging [17].) For experiments with lower \mathcal{A}_f associated with moderate, relatively wide fingering [red diamonds in Fig. 2(a)], the focusing mechanism is dominant and choking is promoted. Note that in the majority of the parameter space examined neither the experiments nor the simulations choked [black circles in Fig. 2(a)].

In our study of two-phase flow in a confined soft Hele-Shaw cell, we found no evidence that viscous fingering is significantly suppressed as it is in an unconfined soft flow cell [10]. Moreover, the well-defined choking behavior observed for single-phase flow [11] may be either suppressed or promoted by the presence of the instability, compared with an analogous axisymmetric system. Thus, the system studied here exhibits neither of the core characteristics of its parent systems. It is also quite distinct from elastic fingering [18] and fingering in viscoelastic fluids [19]. Similar richness of behavior to that observed here can be expected in related multiphase flows interacting with soft components, for example, in soft microfluidics [20] and deformable porous media [21]. We are currently developing more detailed quantitative predictions of fingering and complex fluid-structure interaction near the cell rim in confined soft Hele-Shaw cells, which could directly benefit such practical applications.

The authors would like to acknowledge Yuji Tasaka for the provision of experimental equipment, Nicholas Hawkins and the LIMA Facility Oxford for help with rheometric measurements, and Clive Baker and Martin Quinn for their technical support. F.B. would also like to acknowledge the Royal Society (Grant No. URF/R1/211730). The work of the group from Manchester was funded by the Engineering and Physical Sciences Research Council (EPSRC Grant No. EP/R045364/1). The work of the group from Oxford was funded by the European Research Council under the European Union’s Horizon 2020 Programme (Grant No. 805469), the EPSRC (Grant No. EP/P009751/1), the

John Fell Oxford University Press Research Fund (Grant No. 132/012), and the Maurice Lubbock Memorial Fund.

- [1] E. Jambon-Puillet, M. R. Piéchaud, and P.-T. Brun, Elastic amplification of the Rayleigh-Taylor instability in solidifying melts, *Proc. Natl. Acad. Sci. USA* **118**, e2020701118 (2021).
- [2] M. S. Carvalho and L. E. Scriven, Deformable roll coating flows: Steady state and linear perturbation analysis, *J. Fluid Mech.* **339**, 143 (1997).
- [3] Y. H. Chong, P. H. Gaskell, and N. Kapur, Coating with deformable rolls: An experimental investigation of the ribbing instability, *Chem. Eng. Sci.* **62**, 4138 (2007).
- [4] M. F. Reynolds, K. L. McGill, M. A. Wang, H. Gao, F. Mujid, K. Kang, J. Park, M. Z. Miskin, I. Cohen, and P. L. McEuen, Capillary origami with atomically thin membranes, *Nano Lett.* **19**, 6221 (2019).
- [5] J. Choi, D. Kang, S. Han, S. B. Kim, and J. A. Rogers, Thin, soft, skin-mounted microfluidic networks with capillary bursting valves for chrono-sampling of sweat, *Adv. Healthcare Mater.* **6**, 1601355 (2017).
- [6] H. Lin, J. Tan, J. Zhu, S. Lin, Y. Zhao, W. Yu, H. Hojaiji, B. Wang, S. Yang, X. Cheng, Z. Wang, E. Tang, C. Yeung, and S. Emaminejad, A programmable epidermal microfluidic valving system for wearable biofluid management and contextual biomarker analysis, *Nat. Commun.* **11**, 4405 (2020).
- [7] T. J. Jones, E. Jambon-Puillet, J. Marthelot, and P.-T. Brun, Bubble casting soft robotics, *Nature (London)* **599**, 229 (2021).
- [8] J. Sheng, *Modern Chemical Enhanced Oil Recovery: Theory and Practice* (Gulf Professional Publishing, Amsterdam, 2010).
- [9] A. R. White and T. Ward, CO₂ sequestration in a radial Hele-Shaw cell via an interfacial chemical reaction, *Chaos*. **22**, 037114 (2012).
- [10] A. Juel, D. Pihler-Puzović, and M. Heil, Instabilities in blistering, *Annu. Rev. Fluid Mech.* **50**, 691 (2018).
- [11] F. Box, G. G. Peng, D. Pihler-Puzović, and A. Juel, Flow-induced choking of a compliant Hele-Shaw cell, *Proc. Natl. Acad. Sci. USA* **117**, 30228 (2020).
- [12] See Supplemental Material at <http://link.aps.org/supplemental/10.1103/PhysRevFluids.7.L062001> for more details on experiments, theoretical modeling, and comparison between theory and experiments.
- [13] L. Paterson, Radial fingering in a Hele-Shaw cell, *J. Fluid Mech.* **113**, 513 (1981).
- [14] J. A. Miranda and M. Widom, Radial fingering in a Hele-Shaw cell: A weakly nonlinear analysis, *Physica D* **120**, 315 (1998).
- [15] Y. Couder, Viscous fingering as an archetype for growth patterns, in *Perspectives in Fluid Dynamics*, edited by G. K. Batchelor, H. K. Moffatt, and M. G. Worster (Cambridge University, New York, 2000), pp. 53–104.
- [16] G. G. Peng, D. Pihler-Puzović, A. Juel, M. Heil, and J. R. Lister, Displacement flows under elastic membranes. Part 2: Analysis of interfacial effects, *J. Fluid Mech.* **784**, 512 (2015).
- [17] T. G. J. Chandler, Mathematical Models of Two-Dimensional Sheets and Foundations, Ph.D. thesis, University of Oxford, 2021.
- [18] B. Saintyves, O. Dauchot, and E. Bouchaud, Bulk Elastic Fingering Instability in Hele-Shaw Cells, *Phys. Rev. Lett.* **111**, 047801 (2013).
- [19] B. Saintyves, S. Mora, and E. Bouchaud, A meniscus fingering instability in viscoelastic fluids, *Phys. Fluids* **31**, 063108 (2019).
- [20] H. A. Stone, Tuned-in flow control, *Nat. Phys.* **5**, 178 (2009).
- [21] S. Lee, J. Lee, R. Le Mestre, F. Xu, and C. W. MacMinn, Migration, trapping, and venting of gas in a soft granular material, *Phys. Rev. Fluids* **5**, 084307 (2020).

Trapping and Escape of Viscous Fingers in a Soft Hele-Shaw Cell

Supplementary Material

Gunnar G. Peng,^{1,2} Callum Cuttle,³ Finn Box,² Jian Hui Guan,^{3,4} Anne Juel,² Chris MacMinn,³ and Draga Pihler-Puzović²

¹*Department of Mathematics, Imperial College, Exhibition Road, London SW7 2BX, UK*

²*Department of Physics & Astronomy and Manchester Centre for Nonlinear Dynamics, University of Manchester, Oxford Road, M13 9PL, Manchester, UK*

³*Department of Engineering Science, University of Oxford, Parks Road, Oxford, OX1 3PJ, United Kingdom*

⁴*Department of Mathematics, The University of North Carolina at Chapel Hill, Chapel Hill, North Carolina, USA*

(Dated: April 25, 2022)

S1. EXPERIMENTAL METHODS

The soft slabs were fabricated from PDMS (Sylgard, Farnell). For group A with Sylgard 527, the base polymer and catalyst were mixed in a 1:1 ratio, degassed in a vacuum chamber and then left to cure between one and three weeks at room temperature inside rigid circular molds of inner radius $R_o = 60$ mm and 15 mm frame (made from plastic) that were glued to a glass base plate. A similar procedure was followed for group B with Sylgard 184, except the base polymer and catalyst were mixed in a 1:50 ratio to achieve the low values of G on the order of kPa, and the mould's dimensions were $R_o = 95$ mm and 12 mm frame (made from aluminium). The mould depth was in the range $3 \text{ mm} \leq d \leq 15 \text{ mm}$, resulting in soft slabs with aspect ratio $4 \leq \mathcal{A}_s = R_o/d \lesssim 24$. Once the elastomers were cross-linked, they adhered to the inner boundaries of the rigid moulds. As the substrates aged, their shear modulus G changed with time. This evolution was measured on separate test slabs in an oscillatory rheometer (Kinexus Pro+, Malvern Panalytic for group A and MCR301, Anton Paar for group B) over the course of a month, resulting in an empirical aging formula which was then used to calculate the value of G appropriate for each experiment. We measured the shear modulus in the range $0.94 \text{ kPa} \leq G \leq 4.8 \text{ kPa}$.

Since the soft wall was made from PDMS, we used glycerol as the viscous liquid in our experiments, because it is immiscible with the PDMS and did not swell the soft substrate. Glycerol only partially wetted the walls of the Hele-Shaw cell. However, behind the moving interface, the expanding bubble deposited a continuous film of viscous fluid on the cell boundaries. Dewetting of the film was only observed in experiments performed with low $\mathcal{F}/\mathcal{A}_s$ or after the cell choked (see Fig. 1 of the manuscript, for example), and then only so far behind the moving interface that its influence on the fingering instability is assumed to be negligible. In case of dewetting, far behind the interface thin films on the cell walls would break up and partially retract, forming thicker layers of fluid on the cell boundaries (see the darker blue regions forming behind the interface in the final two images of Figure 1(b) in the main text). As glycerol absorbs water

with high affinity, we measured its viscosity before each batch of experiments using the same shear rheometer as above (group A), or with a custom pipe rheometer (group B). The viscosity of glycerol was found to be in the range $0.23 \text{ Pa s} \leq \mu \leq 1.38 \text{ Pa s}$, while its surface tension was assumed to be $\gamma = 63 \text{ mN/m}$.

The initial separation distance, $0.16 \text{ mm} \leq b \leq 2 \text{ mm}$, between the soft substrate and the overlying glass plate was set by spacers (giving gap aspect ratios $30 \leq \mathcal{A}_f = R_o/b \lesssim 594$). Gas was injected into the pre-filled cell through a port in the centre of the glass plate at nominal volumetric flow rates in the range $1 \leq Q_0 \leq 530 \text{ mL/min}$. For group A, the flow source was a compressed nitrogen cylinder, whose flow rate was set manually by a fine needle valve and monitored using a mass airflow meter (Red-Y Smart Meter PCU1000, Icenta Controls Ltd). A three-way pneumatic solenoid valve was used to switch the gas flow from exiting into the atmosphere to entering the cell at the start of each experiment. The volume V_0 of tubing between the needle valve and the cell was calculated, for use in the modelling of the gas compression. For group B, the flow source was a syringe pump (AL-4000, World Precision Instruments) fitted with a Gastight syringe (1050, Hamilton), connected to the cell port using tubing, and the total volume V_0 in the pump chamber and the tubing was recorded.

The full list of parameters for each experiment is shown in Table S1.

The evolution of the air-liquid interface was recorded in plan view by a digital camera (Nikon D7100, 25 frames per second for group A; Basler Ace acA4096-30um, 6.5–15 frames per second, depending on injection rate and cell volume, for group B). Each experiment was classified as choking or non-choking based on whether or not the soft wall made contact with the base plate.

For group B, the recorded videos were also processed using a light-attenuation method. The initial liquid in the cell was dyed, so that, in each frame of the video, at each pixel the thickness of the liquid layer could be inferred from the light intensity. Ahead of the expanding interface, where the cell is filled with liquid, the measured thickness yields the deformation of the soft wall, after subtraction of the original thickness. Behind the expanding interface, the measured thickness is the thick-

ness of the thin films deposited on the walls. Integrating equation, the thickness over all pixels in the cell yields the total volume of fluid remaining in the cell.

Due to the injected gas compressing, the actual volume flow rate $Q(t)$ of liquid being displaced by the gas and exiting the cell varied (as illustrated in Fig. 2 of the manuscript). To measure $Q(t)$ in each experiment, we employed up to three different methods.

Firstly, for group B, $Q(t)$ can be obtained as the time derivative of the remaining volume of fluid in the cell, as measured using the light-attenuation method.

Secondly, for group B and some of group A, we recorded the bubble pressure $p_b(t)$ relative to the atmospheric pressure using Honeywell pressure sensors in the range of up to 15 PSI, and used an isothermal model for the gas compression to obtain an approximation of $Q(t)$. The relationship between the volume $V_b(t)$ and (gauge) pressure $p_b(t)$ in the gas region is given by $V_b(t) = V_a(1+p_b(t)/p_a)^{-1}$, where V_a is the uncompressed volume of the gas and p_a is atmospheric pressure. For group A where the flow is driven by gas injection via a constricting valve, the uncompressed gas volume downstream of the valve increases as $V_a = V_0 + Q_0 t$ and the flow rate is given by

$$Q = \frac{dV_b}{dt} = \frac{d}{dt} [(V_0 + Q_0 t)(1 + p_b(t)/p_a)^{-1}]. \quad (\text{S1a})$$

For group B where the flow is driven by a syringe pump, the total uncompressed gas volume stays constant at $V_a = V_0$ and the flow rate is given by

$$Q = Q_0 + \frac{dV_b}{dt} = Q_0 + \frac{d}{dt} [V_0(1 + p_b(t)/p_a)^{-1}]. \quad (\text{S1b})$$

Thirdly, for all experiments, we used a travelling-wave analysis to obtain an approximation of the flow rate from the interface position data: At each point on the interface, the local normal velocity of the interface is extracted from the video. Assuming that the velocity evolves slowly with time, the deformation is approximately steady in a travelling-wave frame of reference moving with the interface. Calculating this local solution numerically yields a prediction for the local amount of liquid being displaced by the advancing meniscus, or equivalently the thickness of the liquid films deposited behind. Integrating around the perimeter yields the total rate of fluid displaced by the bubble and hence leaving the cell.

S2. MATHEMATICAL MODEL

We use an axisymmetric depth-averaged model for the flow in the cell, split into two regions separated by the bubble tip $r = r_f(t)$. In the bubble region $0 < r < r_f$ the pressure is spatially uniform, $p(r, t) = p_b(t)$, while in the liquid region $r_f < r < R_o$ the vertical deformation $w_f(r, t)$ of the cell evolves according to the lubrication

$$\frac{\partial w_f}{\partial t} = \frac{1}{r} \frac{\partial}{\partial r} \left(r \frac{(b + w_f)^3}{12\mu} \frac{\partial p}{\partial r} \right). \quad (\text{S2})$$

The interfacial conditions at the meniscus $r = r_f^+$ are

$$(1 - f_1)\dot{r}_f = -\frac{(b + w_f)^2}{12\mu} \frac{\partial p}{\partial r}, \quad (\text{S3a})$$

$$p_b - p = \frac{2\gamma}{b + w_f}(1 + f_2) + \frac{\gamma}{r_f}, \quad (\text{S3b})$$

and depend on the capillary number $Ca = \mu\dot{r}_f/\gamma$ via the functions

$$f_1(Ca) = \frac{Ca^{2/3}}{0.76 + 2.16 Ca^{2/3}}, \quad (\text{S3c})$$

$$f_2(Ca) = \frac{Ca^{2/3}}{0.26 + 1.48 Ca^{2/3}} + 1.59 Ca, \quad (\text{S3d})$$

which measure the thickness of the films deposited behind the tip and the additional viscous pressure drop due to the deposition flow [1]. For the elastic slab in the domain $0 < r < R_o$, $0 < z < d$, the deformation \mathbf{u}^s and stress σ^s are modeled using the equations of linear elasticity, which are formulated with an auxiliary variable $p^s = -\text{Tr}(\sigma^s)/3$ in order to avoid a singularity in the incompressible case $\nu = 1/2$,

$$\sigma^s = -\frac{3\nu}{1-\nu} p^s \mathbf{1} + G(\nabla \mathbf{u}^s + \nabla \mathbf{u}^{sT}), \quad (\text{S4a})$$

$$\nabla \cdot \mathbf{u}^s + \frac{3(1-2\nu)}{2(1+\nu)} \frac{p^s}{G} = 0, \quad (\text{S4b})$$

$$\mathbf{0} = \nabla \cdot \sigma^s = -\frac{3}{2(1+\nu)} \nabla p^s + G \nabla^2 \mathbf{u}^s. \quad (\text{S4c})$$

No-slip conditions $\mathbf{u}^s = \mathbf{0}$ are applied on the mold at $r = R_o$ and at $z = d$, and symmetry conditions $u_r^s = \partial u_z^s / \partial r = 0$ on the axis $r = 0$. On the surface $z = 0$, the surface deformation and normal stress are coupled to the fluid, $u_z^s = w_f$ and $\sigma_{zz}^s = -p$, while the shear stress from the fluid is neglected, $\sigma_{rz}^s = 0$.

We impose the volumetric flow rate of liquid leaving the cell as

$$Q(t) = -2\pi R_o \frac{b^3}{12\mu} \frac{\partial p}{\partial r} \Big|_{r=R_o}. \quad (\text{S5})$$

Due to the mold sidewall having a thickness ℓ_{rim} , imposing zero (i.e. atmospheric) pressure at the outside of the mold results in the outflow pressure at the end of the computational domain being

$$p(R_o, t) = \frac{12\mu Q}{2\pi b^3} \ln \frac{R_o + \ell_{rim}}{R_o}. \quad (\text{S6})$$

The governing equations were solved numerically using a finite-difference method on a grid with spacing $0.02d$, with implicit time-stepping using Newton iteration and an adaptive step size. (Doubling the resolution changed the results by approximately 2%.)

	d (mm)	b (mm)	G (kPa)	μ (Pa s)	V_0 (ml)	Q_0 (ml/min)
Group A $R_o = 60$ mm $\nu = 0.5$ $\gamma = 63$ mN/m $\ell_{rim} = 15$ mm	15	2	1.36	0.72	15	50, 100, 150, 200, 250, 300, 350, 400, 450
	15	1.5	1.02	0.73	15	50, 100
	10	2	1.02	0.23	20	50, 100, 150
			1.06	0.68	20	200, 300, 400, 500, 540
	10	1.5	1.34	0.72	15	50, 100, 150
	7	1.5	1.15	0.8	20	50, 100, 200, 300, 400, 500
	7	1.42	1.02	0.75	15	20, 50, 100, 150, 200, 250
	5	1.5	0.94	0.79	20	50, 100, 150, 200
			0.98	0.83	20	250, 300, 350, 400, 450, 500, 540
	5	1	1.33	0.65	15	100, 200, 300
3	1	1.62	0.72	15	100, 200, 300, 400, 530	
3	0.52	1.62	0.72	15	100, 200	
Group B $R_o = 95$ mm $\nu = 0.5$ $\gamma = 63$ mN/m $\ell_{rim} = 12$ mm	4	0.453	2.9	0.95	43	1
		0.462	2.9	1.03		10
		0.459	3.1	1.12		30
		0.463	3.1	1.15		90
	4	0.325	3.1	1.11	32	4.5
		0.342	3.9	1.38		13.5
		0.332	3.9	1.09		26.8
		0.331	3.9	1.06		48.9
		0.330	3.9	1.04		81.4
	4	0.164	3.9	1.01	32	11.1
		0.164	4.2	1.00		25.5
		0.153	4.8	0.82		37.5
		0.160	4.2	1.02		49.4

TABLE S1. Parameter values used in the experiments shown in Fig. 2 of the manuscript. In group B, the nominal values of b were 0.45, 0.32 and 0.16 mm, and the table shows the average value as measured by the light attenuation method.

S3. FINGERING SUPPRESSES CHOKING

Fig. S1 shows a direct comparison between experiments and numerics for group B, which illustrates the enhanced suppression of choking due to fingering. Fig. S1(a) shows the time-evolution of the maximum plate deflection measured at the bulge, $\max(-w_f)$, normalised by the initial gap thickness b (for experiments, the azimuthal average of $-w_f(r, \theta)$ around the entire cell was used to measure $\max(-w_f)/b$). In all cases shown, the numerics (solid lines) predict choking, while we observe no choking in the experiments (symbols). Until just before the instant of numerical choking, $\max(-w_f)/b$ shows strong agreement between experiments and numerics, consistent with the assumption that choking behaviour should depend only on flow rate while the interface is still far ($\gg d$) from the boundary layer at the rim, see also [2]. By contrast, the maximum interface position relative to the inlet $\max(r_f(\theta))$ (normalised by slab depth d) shows strong divergence [Fig. S1(b)], with the experimental interfaces extending much closer to the rim (marked with the dashed line) than the corresponding

circular interfaces in numerics due to viscous fingering. The values of $\max(r_f)/d$ at the final time of the simulations (i.e., when the cell chokes in numerics), r_{fin} , are indicated in Fig. S1(b) by crosses and large triangles for numerics and experiments, respectively. These interfacial positions are then plotted in Fig. S1(c) as a function of nondimensional nominal flow rate $\mathcal{F}_0/\mathcal{A}_s$, and the data is extended to include all experiments from group B (see table S1). This includes some data, for which neither the experiments nor the simulations choked, so the corresponding final times are when the interface escaped the experimental cell, and the experimental r_{fin}/d reported in Fig. S1(c) is approximately equal to R_o/d . In these cases, we use circles for experiments in Fig. S1(c), and triangles are used otherwise. As illustrated in Fig. S1(c), the experimental interfaces are closer to the rim by a factor of 1.6-2.4 than the numerical interfaces at the instant of choking (or escape), and typically within $O(d)$ of the rim (most are within 6-8 d). The above observations all corroborate the existence of the proximity mechanism by which fingering suppresses choking, as presented in the main document.

[1] G. G. Peng, D. Pihler-Puzović, A. Juel, M. Heil, and J. R. Lister, Displacement flows under elastic membranes. Part

2: Analysis of interfacial effects, J. Fluid Mech. **784**, 512 (2015).

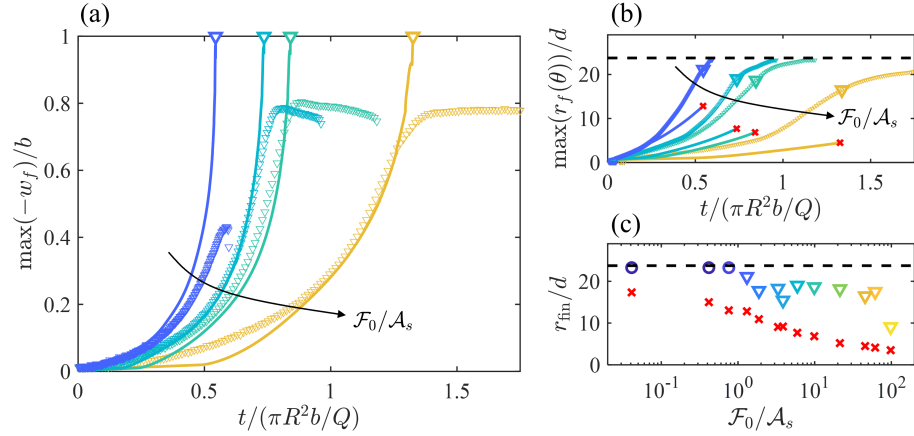


FIG. S1. (a-b) Direct comparison between experiments (symbols) and numerics (solid lines) for the parameters given in rows 3, 8, 9 and 11 of group B in Table S1. (a) Maximum deformation $\max(-w_f)$ near the rim of the soft plate normalised by the relaxed gap b as a function of normalised time. (b) Maximum radial coordinate $\max(r_f(\theta))$ of the interface normalised by relaxed slab depth d as a function of normalised time. Arrows indicate increasing nondimensional nominal flow rate $\mathcal{F}_0/\mathcal{A}_s$. For clarity, the time axis is truncated before the highest flow rate experiment ended. (c) Maximum interface position at the time of choking in the numerics or, when neither the experiments nor the simulations choke, escape in the experiments, r_{fin} , normalised by d as a function of $\mathcal{F}_0/\mathcal{A}_s$ for experiments (large open symbols) and numerics (red crosses) in group B. Triangles indicate experiments that did not choke while the corresponding numerics did, and circles are used for experiments if neither the experiments nor the simulations choked. In (b-c), horizontal dashed lines indicate the edge of the soft plate, $r/d = R_o/d$.

- 209 [2] F. Box, G. G. Peng, D. Pihler-Puzović, and A. Juel, Flow-
 210 induced choking of a compliant Hele-Shaw cell, Proc. Natl.
 211 Acad. Sci. , 202008273 (2020).